Orbital
The electronic journal of chemistry

the electronic journal of chemistry

Full Paper | http://dx.doi.org/10.17807/orbital.v14i1.1670

Synthesis, X-Ray Diffraction (XRD), Differential Thermal Analysis (DTA), and Scanning Electron Microscopy (SEM) of the Alloy $(CuInTe_2)_{1-x}(NbTe)_x$ with x=0.5

Gerzon E. Delgado * [a], Miguel Palmera [b], Pedro Grima-Gallardo [b,c] and Miguel Quintero [c]

A polycrystalline ingot (30mm long, 10mm diameter) of the alloy $(CuInTe_2)_{1-x}(NbTe)_x$ with x=0.5 has been produced using the melt and anneal technique and characterized by X-Ray Diffraction (XRD), Diferential Thermal Analysys (DTA) and Scanning Electron Microscopy (SEM). From XRD results, and using Rietveld refinement method, the crystal structure has been obtained indicating than this alloy crystallizes in a chalcopyrite-like structure, space group $P\bar{4}2c$ (Nº 112), unit cell parameters a = 6.1933(2) Å, c = 12.4293(2) Å, V = 476.75(2) Å^3, figures of merit R_{exp}= 6.7%, R_p= 7.5%, R_{wp}= 7.3%, and S = 1.1. DTA measurements indicate three thermal transitions at 1028, 977 and 886 K in the heating cycle, and 1016, 900 and 848 K in the cooling. The transitions at 1028 and 1016 correspond to the melting and solidification point, respectively; the transitions at 977 and 900 K are of solid to liquid+solid type, whereas the transitions at 886 and 848 K correspond to order-disorder. The melting point is incongruent. In the diffraction pattern, traces of a secondary phase are observed; this phase has been identified using SEM technique as $(CuIn)_{0.5}NbTe_2$.

Graphical abstract

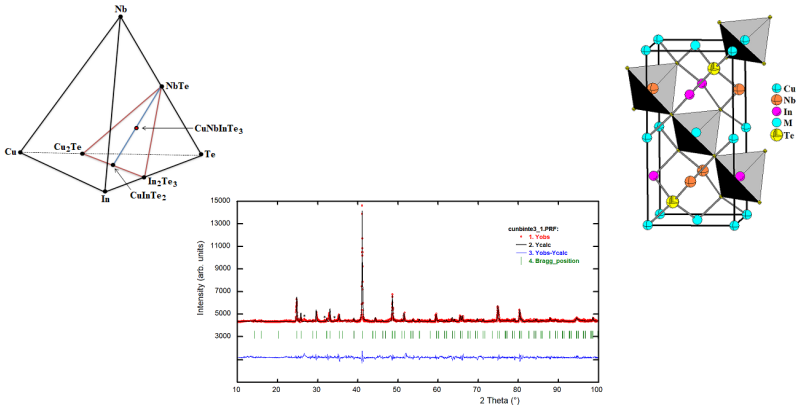

Keywords

Chalcogenide alloys
Superconductor
Thermal analysis
Crystal structure
Powder X-ray diffraction
Rietveld method

Article history

Received 30 October 2021
Revised 08 February 2022
Accepted 17 February 2022
Available online 26 March 2022

Handling Editor: Cauê A. Martins

1. Introduction

The use of semiconductor materials to convert industrial waste heat into electricity is the main objective of thermoelectric technology [1]. Materials that display these properties are called Thermoelectric Materials (TE) and can directly convert heat into electricity or vice versa, the reason why have been recently studied. Chalcogenides containing copper as univalent cation has received growing interest as promising thermoelectric materials due to their great

[a] Laboratorio de Cristalografía, Departamento de Química, Facultad de Ciencias, Universidad de Los Andes, Mérida 5101, Venezuela. [b] Centro Nacional de Tecnologías Ópticas (CNTO) y Centro Investigaciones de Astronomía (CIDA), Mérida 5101, Venezuela. [c] Centro de Estudios en Semiconductores, Departamento de Física, Facultad de Ciencias, Universidad de Los Andes, Mérida 5101, Venezuela. Corresponding author. E-mail: **gerzon@ula.ve**

elemental abundance, low toxicity, and high-level efficiency [2-4]. The efficiency of TE materials is determined by the dimensionless figure of merit, $zT = \alpha^2\sigma T/\kappa$, where α = thermopower, σ = electrical conductivity, T = absolute temperature, and κ = thermal conductivity [4].

Recently, attention has focused on studying the $CuInTe_2$ ternary, a well-known semiconductor with a chalcopyrite structure [5], due to its potential use as an agent in thermoelectric technology with a figure of merit of 1.18 at 850 K, which is better than any other un-doped diamond-like material [6].

In general, chalcopyrite compounds with formula I-III-VI_2 (I = Cu, Ag; III = Al, Ga, In, VI = S, Se, Te) form a broad group of semiconductor materials with diverse electrical and optical properties [7]. These chalcogenide materials crystallize with tetragonal symmetry in the space group $I\bar{4}2d$ (N°122) being isomorphic with the $CuFeS_2$ mineral known as chalcopyrite [8]. If these compounds are alloyed with a II-VI binary, it is possible to form alloys with composition $(I\text{-}III\text{-}VI_2)_{1-x}(II\text{-}VI)_x$, and changing the variable x the following family of materials can be produced, such as: $I_2\text{-}II\text{-}III_2\text{-}VI_5$ (x = ⅓), I-II-III-VI_3 (x = ½), and $I\text{-}II_2\text{-}III\text{-}VI_4$ (x = ⅔). All these phases agree with the rules of formation of adamantane compounds, belong to the normal semiconductor derivatives of the II-VI binary semiconductors and are good candidates for intermediate compounds in the phase diagram [9].

In particular, the families of the $(Cu\text{-}III\text{-}VI_2)_{1-X}(II\text{-}VI)_X$ system with x = ½ has been investigated in our group and since the structural characterization of the $CuFeInSe_3$-type [10] structure, all those that have been synthesized have turned out to be isomorphic, crystallizing in the tetragonal space group $P\bar{4}2c$ with a chalcopyrite-like structure [11]. Table 1 shows the crystallographic information for members of this system reported to date [10-18]. All these materials have been studied for spintronic applications with interesting magnetic, thermal and thermoelectric properties. For the more recent quaternary reported, $CuFeInTe_3$, properties such as super-paramagnetism and as *n*-type thermoelectric material applicable at high temperatures have been found [19,20].

In particular, for the alloy $CuNbInTe_3$ magnetic measurement shown that the incorporation of magnetic Nb-atoms in the diamagnetic $CuInTe_2$ matrix produces a transition to the superconductor state, with a critical temperature T_C = 12 K [21], however, there are no structural reports in the databases Powder Diffraction File [22], Inorganic Crystal Structure Database (ICSD) [23], or Springer Materials [24]. Therefore, in this work the synthesis, thermal analysis, and crystal structure analysis are performed.

Table 1. Structural information reported to date for chalcogenide alloys with formula I-III-IV-VI_3 with I= Cu, II= Mn, Fe, Ni, Zn, Nb, Ta, III= Al, Ga, In, VI= Se, Te. [*] this work. All these phases crystallize in the space group $P\bar{4}2c$.

Compound	*a* (Å)	*c* (Å)	*c*/*a*	V (Å^3)	Cu-Se	II-Se	III-Se	Ref
$CuMnAlSe_3$	5.6034(6)	10.977(1)	1.96	344.66(6)	2.423(8)	2.443(8)	2.397(8)	[12]
$CuMnGaSe_3$	5.6230(4)	11.028(1)	1.96	348.68(5)	2.419(8)	2.452(8)	2.432(8)	[12]
$CuMnInSe_3$	5.7907(5)	11.648(1)	2.01	390.58(8)	2.428(8)	2.448(8)	2.614(8)	[12]
$CuFeAlSe_3$	5.609(1)	10.963(2)	1.96	344.9(1)	2.418(8)	2.462(8)	2.379(8)	[13]
$CuFeGaSe_3$	5.6165(3)	11.075(1)	1.97	349.36(4)	2.421(8)	2.467(8)	2.434(8)	[13]
$CuFeInSe_3$	5.7762(2)	11.5982(7)	2.01	386.97(3)	2.423(8)	2.464(8)	2.602(8)	[10]
$CuNiGaSe_3$	5.6213(1)	11.0282(3)	1.96	348.48(1)	2.419(8)	2.465(8)	2.432(8)	[14]
$CuNiInSe_3$	5.7857(2)	11.6287(5)	2.01	389.26(3)	2.421(8)	2.462(8)	2.614(8)	[14]
$CuZnAlSe_3$	5.6083(2)	10.992(1)	1.96	345.73(4)	2.426(8)	2.451(8)	2.387(8)	[15]
$CuZnGaSe_3$	5.6165(3)	11.075(1)	1.97	351.49(4)	2.426(8)	2.452(8)	2.439(8)	[15]
$CuZnInSe_3$	5.7922(4)	11.658(1)	2.01	391.12(8)	2.429(8)	2.450(8)	2.615(8)	[15]
$CuNbGaSe_3$	5.6199(4)	11.0275(2)	1.96	348.28(4)	2.425(8)	2.445(8)	2.438(8)	[16]
$CuTaInSe_3$	5.7831(1)	11.6227(4)	2.01	388.71(2)	2.438(6)	2.458(6)	2.599(6)	[17]
$CuFeInTe_3$	6.1842(1)	12.4163(2)	2.01	474.85(1)	2.665(1)	2.726(1)	2.746(1)	[18]
$CuNbInTe_3$	6.1933(3)	12.4293(2)	2.01	477.13(5)	2.639(1)	2.756(1)	2.768(1)	[*]

2. Results and Discussion

In Figure 1, the composition representation for the quaternary system Cu-In-Nb-Te is displayed. The red triangle is composed by the Cu_2Te-NbTe, NbTe-In_2Te_3 and Cu_2Te-In_2Te_3 tie lines where it can be noted that the ternary $CuInTe_2$ is located at the center of the Cu_2Te-In_2Te_3 tie line whereas the alloy $CuNbInTe_3$ is at the center of the $CuInTe_2$-NbTe tie line. This type of diagram is useful in order to know if the phases observed belong to the phase diagram or they are impurity phases.

Figure 2 shows the experimental (Y_{obs} in red) powder XRPD pattern of $CuNbInTe_3$. Some peaks with very low intensities cannot be indexed. Bragg positions of the diffraction peaks from this compound are also indicated. The first peak positions of the main phase were successfully indexed using the Dicvol04 program [25] in a tetragonal unit cell with similar parameters to those of the ternary chalcopyrite parent $CuInTe_2$ [5]. A space group search using ExtSym program [26] suggested the space group $P\bar{4}2c$ which is consistent with the systematic absences. $CuNbInTe_3$ is isomorphic with the related quaternary alloys $CuFeInSe_3$ [10] and $CuFeInTe_3$ [18], with a *P*-chalcopyrite structure.

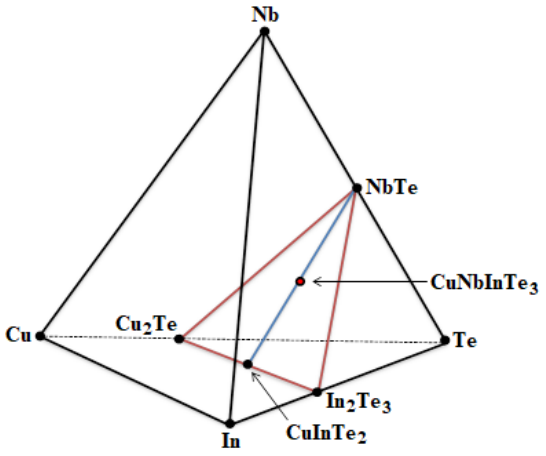

Fig. 1. Compositional representation of the Cu-Nb-In-Te quaternary solid solutions system.

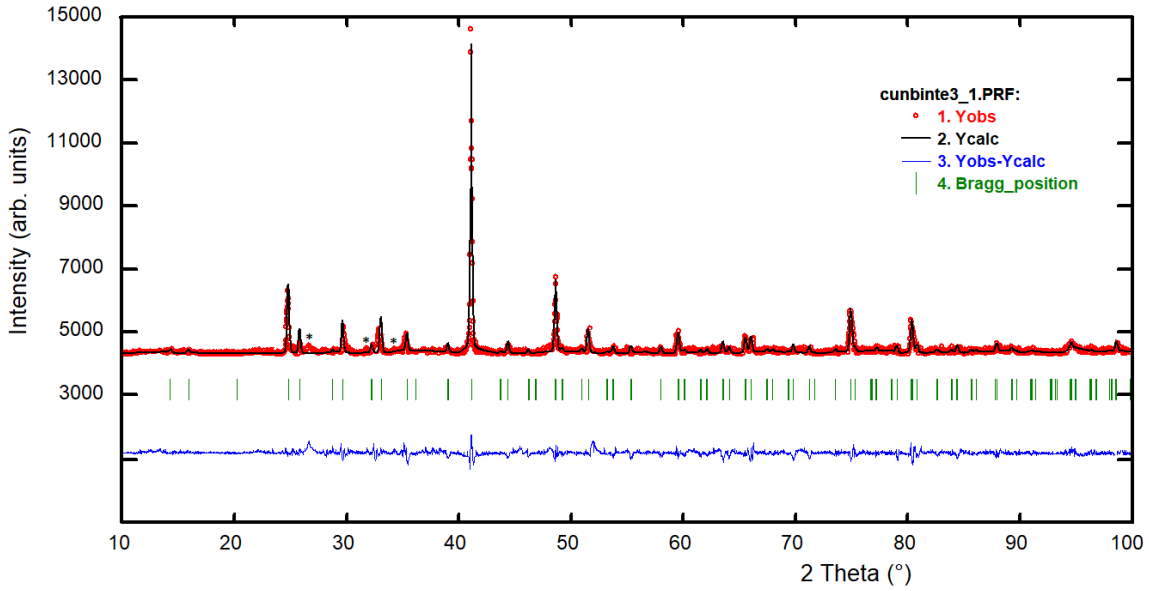

Fig. 2. Rietveld refinement final plot of $CuNbInTe_3$. Unindexed peaks are denoted by asterisks. The lower trace is the difference curve between observed and calculated patterns. The Bragg reflections are indicated by vertical bars.

For the Rietveld refinement [27] of the $CuNbInTe_3$ crystal structure, the more recent version of the Fullprof, version 7.40, March 2021 [28] was used. The atomic coordinates of $CuFeInTe_3$ [18] and the unit cell parameters obtained from the indexed were used in the refinement. Peak shapes were described by the parameterized pseudo-Voight function [29]. The background was described by the automatic interpolation of 67 points throughout the whole pattern. The thermal motion of the atoms was described by one isotropic temperature factor for each type of atom.

A total of 23 parameters of the $CuNbInTe_3$ alloy were refined, including peak shape parameters, scale factor, cell parameters, atomic coordinates, isotropic displacement parameters, and full width at half-maximum (FWHM) parameters.

The final plot of the Rietveld refinement is shown in Figure 2, the calculated powder pattern is shown as a solid black color line, the solid blue line is the difference between the calculated and experimental powder X-ray patterns, and the vertical green lines show expected Bragg diffraction peaks calculated using the space group $P\bar{4}2c$. Table 2 summarizes the Rietveld refinement results for $CuNbInTe_3$, and Table 3 shown the atomic coordinates, thermal displacement factors, bond distances, and bond angles. Figure 3 shows the unit cell diagram.

Table 2. Rietveld refinement results for $CuNbInTe_3$.

Chemical formula	$CuNbInTe_3$	**Wavelength (Cu *Kα*) (Å)**	1.5418
Formula weight (g/mol)	386.66	**Range 2θ (°)**	10-100
***a* (Å)**	6.1933(2)	**Step size (°)**	0.02
***c* (Å)**	12.4293(2)	**Counting Time (s)**	40
***V* (Å³)**	476.75(2)	**N° intensities**	4501
c/a	2.01	**Independent reflections**	322
System	tetragonal	R_{exp} **(%)**	6.7
Space group	$P\bar{4}2c$ (N° 112)	R_p **(%)**	7.5
Z	8/3	R_{wp} **(%)**	7.3
ρx (g cm^{-3})	6.074	***S***	1.1

R_{exp}= 100 $[(N\text{-}P+C)/\sum_w(y_{obs}^2)]^{1/2}$ N-P+C is the number of degrees of freedom
R_p= 100 $\sum|y_{obs}\text{-}y_{calc}|/\sum|y_{obs}|$ R_{wp}= 100 $[\sum_w|y_{obs}\text{-}y_{calc}|^2/\sum_w|y_{obs}|^2]^{1/2}$ S= $[R_{wp}/R_{exp}]$

The quaternary superconductor alloy $CuNbInTe_3$, bellowing to the system $(CuInTe_2)_{1\text{-}X}(NbTe)_X$ with composition x = ½, crystallize in the tetragonal space group $P\bar{4}2c$ with a $CuFeInSe_3$-type structure. In this *P*-chalcopyrite structure [11], the addition of a new cation, as a transition metal, to a ternary chalcopyrite structure leads to symmetry reduction from an ordered chalcopyrite structure $I\bar{4}2d$ to a related $P\bar{4}2c$ with a partially disorder cation distribution [10]. This alloy has a normal adamantine-structure and can be described as a derivative of the sphalerite structure [9], where each cation is coordinated by four anions (Te) and each anion is coordinated by four cations (one Cu, one Nb, one In, and one M) located at the corners of a slightly distorted tetrahedron.

Bond distances in Table 3 show a Cu-Te bond length of 2.639(1) Å, Nb-Te of 2.756(1) Å, and In-Te of 2.768(1) Å. These lengths compare well to those found for the related ternary adamantine structures: $CuInTe_2$ [(2.5881(3)-2.7878(3) Å] [5], $CuNbTe_2$ [average 2.626(7)-2.861(5) Å] [30], Cu_3NbTe_4

[(2.588(4)-2.633(4) Å] [31], $AgIn_5Te_8$ [32], $AgInTe_2$ [33], $Cu_3In_5Te_9$ [34], $Cu_3In_7Te_{12}$ [35], and quaternaries: $CuTa_2InTe_4$ [36], $CuCo_2InTe_4$ and $CuNi_2InTe_4$ [36], and $CuFeInTe_3$ [18].

Table 3. Atomic coordinates, isotropic temperature factor, and selected geometric parameters (Å, °) for $CuNbInTe_3$, derived from the Rietveld refinement. Bond valence sum (BVS) results are shown. M = (⅓Cu+⅓Nb+⅓In).

Atom	Ox.	BVS	Wyck.	*x*	*y*	*z*	foc	B (Å²)
Cu	+1	1.38	2*c*	0	½	¼	1	0.5(1)
Nb	+2	2.53	2*e*	0	0	0	1	0.7(1)
In	+3	3.24	2*b*	½	0	¼	1	0.6(1)
M			2*f*	½	½	½	1	1.0(1)
Te	-2	2.31	8*n*	0.2532(1)	0.2560(1)	0.1173(1)	1	1.5(1)

Cu - Te		2.639(1)		Nb - Te		2.756(1)		In - Te^{i}		2.768(1)	
Te^{ii} - Cu - Te^{iii}		107.7(1)	x4	Te - Nb - Te^{v}		111.1(1)	x4	Te^{i} - In - Te^{vii}		110.7(1)	x4
Te^{ii} - Cu - Te^{iv}		112.6(1)	x2	Te - Nb - Te^{vi}		105.5(1)	x2	Te^{i} - In - Te^{viii}		106.3(1)	x2

Symmetry codes: (i) 0.5-x, 0.5-y, 0.5+z; (ii) y, x, z; (iii) 0.5-x, 0.5+y, 0.5-z; (iv) -y, 1-x, z; (v) -x, -y, z; (vi) y, -x, -z; (vii) 0.5-y, -0.5+x, 0.5-z; (viii) -0.5+x, -0.5+y, 0.5+z. Bond valence sum (BVS): $V_{ij}= \sum_j \exp[(R_o-R_{ij})/b]$, b= 0.37 Å, r_o(Cu-Te)= 2.27 Å, r_o(Nb-Te)= 2.60 Å , r_o(In-Te)= 2.69 Å

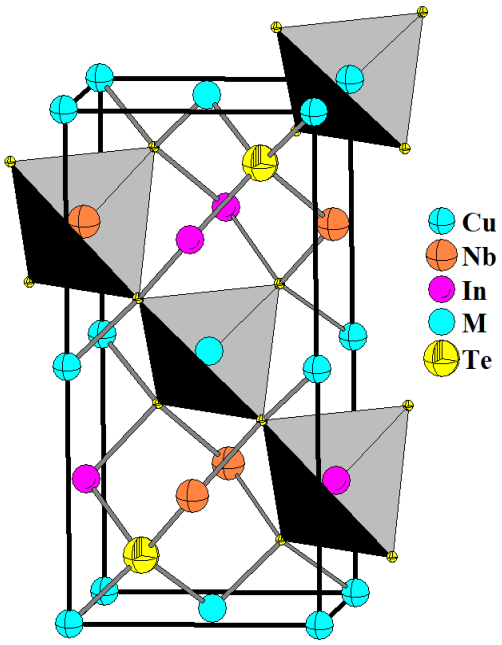

Fig. 3. Unit cell diagram of the quaternary $CuNbInTe_3$ ($P\bar{4}2c$) structure showing the tetrahedra around the Cu^{1+}, Nb^{2+}, and In^{3+} cations.

The chemical structure was validated using the Bond Valence Sum (BVS) calculations based on bond-strength examination [38,39]. These calculations use the Brown-Altermatt empirical expression, $V_{ij} = \exp[(R_o-d_{ij})/B$, where d_{ij} is the interatomic distance and B is taken to be a "universal" constant equal to 0.37 Å. The values for the reference distance R_o are 2.27 Å, 2.53 Å, and 2.69 Å, for Cu-Te, Fe-Te, and In-Te, respectively [39]. The calculated oxidation states agree with the expected formal oxidation states for Cu^{1+}, Nb^{2+}, In^{3+}, and Te^{2-} ions, whose results can also be seen in Table 3.

In Figure 4, the DTA thermogram is displayed. Measurements indicate three thermal transitions at 1028, 977 and 886 K in the heating cycle, and 1016, 900 and 848 K in the cooling. The transitions at 1028 and 1016 correspond to the melting and solidification point, respectively; the transitions at 977 and 900 K are of solid to liquid+solid type, whereas the transitions at 886 and 848 K correspond to order-disorder. The melting point is incongruent.

Based on heating and cooling cycles, the sequence of transitions can be explained as follows (Scheme 1):

Scheme 1. Phase transitions in the DTA analysis of $CuNbInTe_3$.

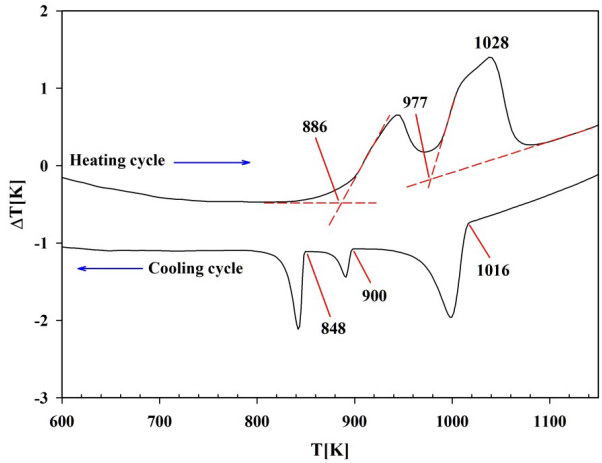

Fig. 4. DTA thermogram for $CuNbInTe_3$ showing heating and cooling cycles. The dashed red lines show the criteria (intersection of the baseline with the slope of the peak) for the transition temperatures. The red solid lines signal the transition temperature values.

At T<848 K, solid 1 is a semi-ordered phase, s.g. $P\bar{4}2c$, where cations are partially disordered. In the temperature interval, 848 K < T < 900 K, solid 1 goes to solid 2 where a complete disorder of the cations occurs; solid 2, possibly shows a sphalerite structure, s.g. $F\bar{4}3m$, in analogy with $CuInTe_2$. At 900 K, solid 2 melt incongruently given place to a relatively wide (106 K) solid + liquid region. Finally, at 1016 K, all the solid phase becomes liquid.

For a more exhaustive analysis of the $CuNbInTe_3$ alloy, SEM measurements were performed on a thin disk (1mm

think, 10mm diameter) cut from the center of the ingot. Although, much of the sample is composed by a chalcopyrite-like phase with stoichiometry given in Table 4, in some parts the sample another phase had been identified with stoichiometry close to $(CuIn)_{0.5}NbTe_2$, which can also be written as $CuInNb_2Te_4$ (Table 4). This phase corresponds to the $(CuInTe_2)_{1-x}(NbTe)_x$ alloy system with x=2/3; then, this phase, $CuInNb_2Te_4$, belongs to the phase diagram.

In Figure 5, the fluorescence spectrum and the atom distribution are given. We can observe that the atom distribution is quite homogeneous.

Table 4. SEM experimental results for the sample $CuNbInTe_3$.

Composition	MW (g)	Nominal Stoichiometry (%)	Experimental Stoichiometry (%)
$CuNbInTe_3$	654.07	Cu = 16.67 Nb = 16.67 In = 16.67 Te = 50.00	Cu = 15.4 ± 0.2 Nb = 16.2 ± 0.2 In = 15.5 ± 0.2 Te = 51.9 ± 0.5
$CuInNb_2Te_4$	874.58	Cu = 12.50 Nb = 25.00 In = 12.50 Te = 50.00	Cu = 13.5 ± 0.7 Nb = 24.7 ± 0.3 In = 11.0 ± 0.2 Te = 50.8 ± 0.6

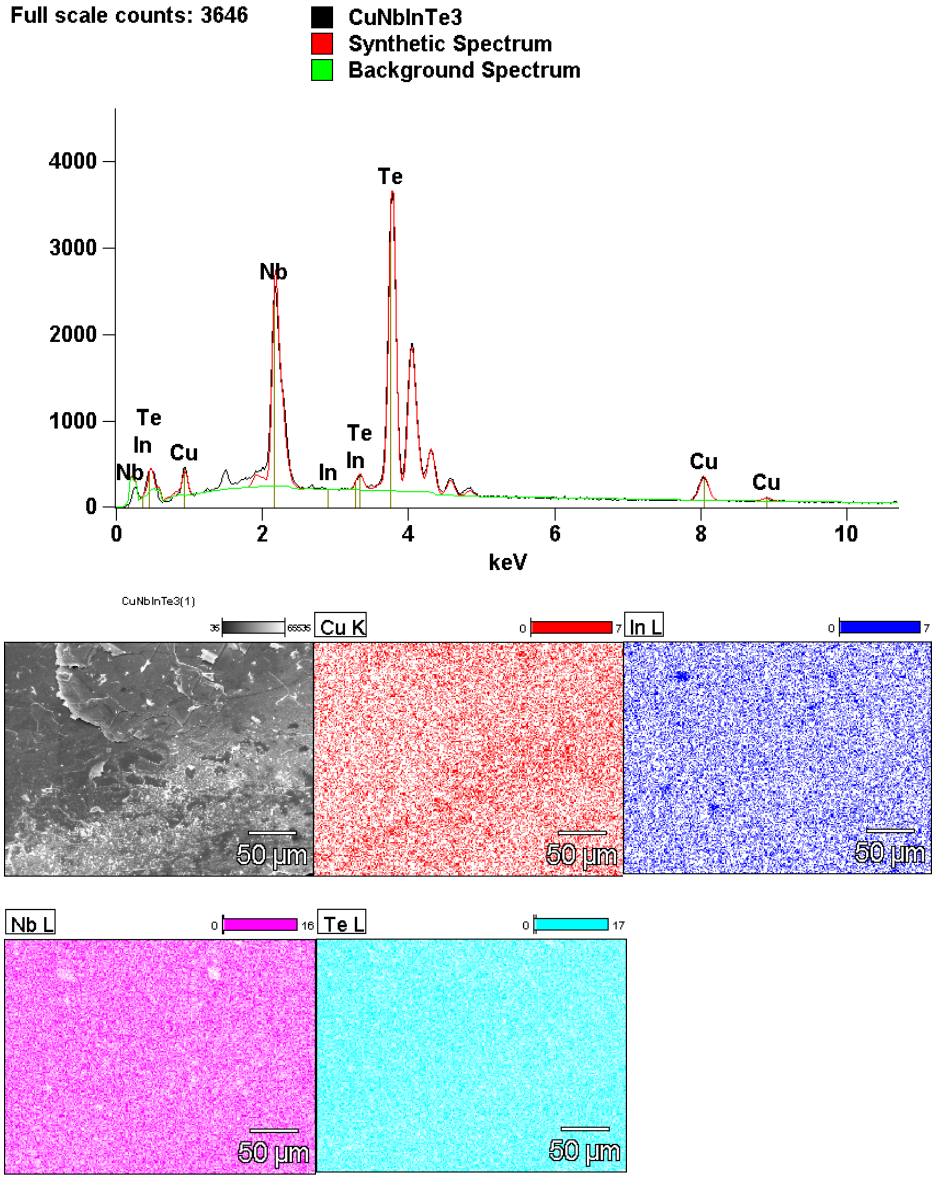

Fig. 5. $CuNbInTe_3$ alloy: fluorescence spectrum and atom distribution.

3. Material and Methods

3.1. Synthesis

A polycrystalline sample (1 g) of nominally $CuNbInTe_3$ was prepared by the melt and anneal technique. Stoichiometric amounts of Cu, Nb, In and Te elements (99.99% of purity, GoodFellow) were charged in an evacuated quartz ampoule, which was previously exposed to pyrolysis to avoid reaction

of the starting materials with quartz. Then, the ampoule was sealed under vacuum and the fusion process was carried out inside a furnace (vertical position) heated up to 1500K at a rate of 20 K/h, with a stop of 48 h at 723K (melting temperature of Te). The ampoule was shaking using a mechanical system during all the heating processes to guarantee the whole mixing of all the elements. The high temperature was keeping for others 48 h with the mechanical shaking system on. Then, the mechanical shaking system was switched off and the temperature was gradually reduced at a rate of 20 K/h, down to 900K. The ampoule was kept at this temperature for 30 days. Finally, the sample was cooled to room temperature at a rate of 10 K/h.

3.2. Scanning Electron Microscopy (SEM)

Stoichiometric relations of the samples were examined by scanning electron microscopy (SEM) technique, using Hitachi S2500 equipment. The microchemical composition was found by an energy-dispersive x-ray spectrometer (EDS) coupled with a computer-based multichannel analyzer (MCA, Delta III analysis, and Quantex software, Kevex). For the EDS analysis, Kα lines were used. The accelerating voltage was 15 kV. The samples were tilted 35 degrees. A standardless EDS analysis was made with a relative error of ± 5-10% and detection limits of the order of 0.3 wt %, where the k-ratios are based on theoretical standards.

3.3. Differential Thermal Analysis (DTA)

Differential Thermal Analysis (DTA) measurements were obtained in the temperature range between 293 K and 1423 K, using a Perkin-Elmer DTA-7 with aluminum and gold used as reference materials. The charge was of the powdered alloy of approximately 100-mg weight. Both heating and cooling runs were carried out on each sample, the average rates of these runs being approximately 10 °C /min. The error in determining these temperatures is about ±10 K.

3.4. Powder X-Ray Diffraction

A sample of $CuNbInTe_3$ was ground in an agate mortar and pestle to a particle size of fewer than 106 μm. Powder X-ray diffraction pattern was collected at room temperature (298 K) on a Philips PW1250 powder X-ray diffractometer operating in Bragg-Brentano geometry using Cu Kα radiation (λ= 1.54056 Å). A tube power of 40 kV and 25 mA was employed. A diffracted beam graphite monochromator and a scintillation detector were used. The scan range was from 10 to 100° 2θ with a step size of 0.02° and a counting time of 50 s/step. Silicon was used as an external standard. For the Rietveld refinement, the whole diffraction data was used.

4. Conclusions

The quaternary alloy $CuNbInTe_3$ was prepared by the melt and annealing method and its crystal structure was refined using powder X-ray diffraction data. This compound crystallizes through a *P*-chalcopyrite fashion with a normal adamantine structure and tetrahedral coordination around cations and anions. The chemical structural was checked by analysis of the interatomic distances using the Bond Valence Sum (BVS) formula based on bond-strength examination. This quaternary alloy melts incongruently at 1028 K. A secondary phase, identified as $(CuIn)_{0.5}NbTe_2$, was also observed.

Acknowledgments

This work was supported by CDCHT-ULA and CONICIT (Grant LAB-97000821).

Author Contributions

Gerzon E. Delgado: Conceptualization, Writing - review & editing, Supervision. Miguel Palmera: Methodology. Pedro Grima-Gallardo: Conceptualization, Writing - review & editing. Miguel Quintero: Methodology.

References and Notes

[1] Zhao, L. D.; Kanatzidis M. G. *J. Materiomics* **2016**, *2*, 101. [Crossref]

[2] Grundmann, M. The physics of semiconductors: An introduction including nanophysics and applications, Springer International Publishing, Switzerland, 2016. [Crossref]

[3] Zhang, D.; Bai, H. C.; Li, Z. L.; Wang, J. L.; Fu, G. S.; Wang, S. L. *Chinese Phys. B* **2018**, *27*, 047206. [Crossref]

[4] Wei, T. R.; Qin, Y.; Deng, T.; Song, Q.; Jiang, B.; Liu, R.; Qiu, P.; Shi, X.; Chen, L. *Sci. China Mater.* **2019**, *62*, 8. [Crossref]

[5] Knight, K. S. *Mater. Res. Bull*. **1992**, *27*, 161. [Crossref]

[6] Liu, R.; Xi, L.; Liu, H.; Shi, X.; Zhang, W.; Chen, L. *Chem. Commun*. **2012**, *48*, 3818. [Crossref]

[7] Jaffe, J. E.; Zunger, A. *Phys. Rev. B* **1984**, *29*, 1882. [Crossref]

[8] Pauling, L.; Brockway, O.L. *Z. Kristallogr*. **1932**, *82*, 1988. [Crossref]

[9] Parthé E. Wurtzite and Sphalerite Structures. In: J.H. Westbrook, R.L. Fleischer (eds), Intermetallic Compounds, Principles and Applications. Vol. 1, John Wiley & Sons, Chichester, UK, 1995.

[10] Mora, A. J.; Delgado, G. E.; Grima-Gallardo, P. *Phys. Stat. Solidi (a)* **2007**, *204*, 547. [Crossref]

[11] Höenle, W.; Kuehn, G.; Boehnke, U. C. *Cryst. Res. Technol*. **1988**, *23*, 1347. [Crossref]

[12] Delgado, G. E.; Mora, A. J.; Contreras, J. E.; Grima-Gallardo, P.; Durán, S.; Muñoz, M.; Quintero, M. *Cryst. Res. Technol*. **2009**, *44*, 548. [Crossref]

[13] Delgado, G. E., Flores-Cruz, J. A.; Grima-Gallardo, P.; Quintero, M.; Moreno, A. *Mater. Res*. **2018**, 29, e20160748. DOI: [Crossref]

[14] Delgado, G. E.; Mora, A. J.; Grima-Gallardo, P.; Durán, S.; Muñoz, M.; Quintero, M. *Bull. Mater. Sci*. **2010**, *33*, 637. [Crossref]

[15] Delgado, G. E.; Grima-Gallardo, P.; Quintero, M. *Rev. Mex. Fís*. **2016**, *62*, 393. [Link]

[16] Flores-Cruz, J. A.; Delgado, G. E.; Contreras, J. E.; Quintero, Nieves, L.; Grima-Gallardo, P. *Tchê Quím. J*. **2018**, *15*, 224. [Link]

[17] Delgado, G. E.; Mora, A. J.; Grima-Gallardo, P.; Durán, S.; Muñoz, M.; Quintero, M. *Cryst. Res. Technol*. **2008**, *43*, 783. [Crossref]

[18] Delgado, G. E.; Grima-Gallardo, P.; Aitken, J. A.; Cabrera, H.; Cisterna, J.; Cárdenas, A.; Brito, I. *Rev. Mex. Fís*. **2021**, *67*, 305. [Crossref]

[19] Grima-Gallardo, P.; Quintero, M.; Nieves, L.; Cabrera, H.; Pérez-Cappé, E.; Zumeta-Dubé, I.; Aitken, J. A.; Brant, J. A. *Rev. Latinoam. Metal. Mater.* **2018**, *38*, 53. [Link]

[20] Cabrera, H.; Zumeta-Dubé, I.; Korte, D.; Grima-Gallardo, P.; Alvarado, F.; Aitken, J. A.; Brant, J. A.; J.H. Zhang, J. H.; A. Calderón, A.; Marín, E.; Aguilar-Frutis, M.; Erazo, J. E.; Perez-Cappe, E.; Franko, M. *J. Alloys Compd.* **2015**, *651*, 490. [Crossref]

[21] Grima-Gallardo, P.; Palmera, M.; Muñoz, S.; Durán, M.; Quintero, E.; Quintero, M.; Nieves, L.; Moreno, E.; Ramos, M. A.; Romero, H. *Adv. Mat. Sci. & Technol.* **2013**, *I7*, 1.

[22] PDF-ICDD, International Centre for Diffraction Data, Newtown Square, PA, USA, 2019.

[23] ICSD, Inorganic Crystal Structure Database, Gemlin Institute, Kalrsruhe, Germany, 2016.

[24] Springer Materials, https://materials.springer.com (2021).

[25] Boultif, A.; Louër, D. *J. App. Cryst*. **2004**, *37*, 724. [Crossref]

[26] Markvardsen, A. J.; Shankland, K.; David, W. I. F.; Johnston, J. C.; Ibberson, R. M.; Tucker, M.; Nowell, H.; Griffin, T. *J. Appl. Cryst*. **2008**, 41, 1177. [Crossref]

[27] Rietveld, H. M. *J. App. Cryst*. **1969**, *2*, 65. [Crossref]

[28] Rodriguez-Carvajal, J. Fullprof (version 7.5), Laboratoire Léon Brillouin (CEA-CNRS), France, **2021**.

[29] Thompson, P.; Cox, D. E.; Hastings, J. B. *J. Appl. Cryst*. **1987**, *20*, 79. [Crossref]

[30] Sörgel, T.; Jansen, M. *Solid State Sci*. **204**, *6*, 1259. [Crossref]

[31] Mora, A. J.; Delgado, G. E.; Pineda, C.; Tinoco, T. *Phys. Status Solidi (a)* **2004**, *201*, 1477. [Crossref]

[32] Delgado, G. E.; Mora, A. J.; Grima-Gallardo, P.; Durán, S.; Muñoz, M.; Quintero, M. *Chalcogenide Lett*. **2009**, *6*, 335. [Link]

[33] Delgado, G. E.; Mora, A. J.; Avila, R.; Paredes, S.; Pineda, C. *Rev. Latinoam. Metal. Mater*. **2015**, *35*, 110. [Crossref]

[34] Delgado, G. E.; Rincón, C.; Marroquín, G. *Rev. Mex. Fis.* **2019**, *65*, 360. [Crossref]

[35] Delgado, G. E.; Guedez, E.; Sanchéz-Pérez, G.; Rincón, C.; Marroquin, G. *Rev. Mater*. **2019**, *24*, e12329. [Crossref]

[36] Delgado, G. E.; Mora, A. J.; Grima-Gallardo, P.; Muñoz, M.; Durán, S.; Quintero, M. *Phys. B*, **2008**, *403*, 3228. [Crossref]

[37] Delgado, G. E.; Grima-Gallardo, P.; Nieves, L.; Cabrera, H.; Glenn, J. R.; Aitken, J. A. *Mater. Res*. **2016**, *19*, 1423. [Crossref]

[38] Brown, I. D.; Altermatt, D. *Acta Cryst. B* **1985**, *41*, 244. [Crossref]

[39] Brese, N. E.; O.'Keeffe, M. *Acta Cryst. B* **1991**, *47*, 192. [Crossref]

How to cite this article

Delgado, G. E.; Palmera, M.; Grima-Gallardo, P.; Quintero, M. *Orbital: Electron. J. Chem.* **2022**, *14*, 33. DOI: http://dx.doi.org/10.17807/orbital.v14i1.1670